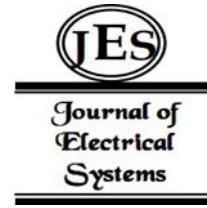[1,*]Yanshen Zhang

[2]Hongfu Qiang

[3]Xueren Wang

[4]Zhejun Wang

[5]Jiaxiang Wang

[6]Huiru Cui

Investigation on A Viscoelastic Creep Damage Constitutive Model for HTPB Propellant and Its Application in Finite Element Analysis

JES
Journal of Electrical Systems

Abstract: - Solid rocket motor (SRM) is typically kept in storage for a significant portion of its lifespan. During storage, the propellant grain creeps under the action of gravity. To investigate the creep properties of hydroyl-terminated polybutadiene (HTPB) propellant under long-term loading, a creep damage constitutive model is developed based on the generalized Kelvin model and continuum damage mechanics theory. Parameters for this model are determined through creep tests conducted on HTPB propellant under various stress levels. Furthermore, to enable the application of the developed propellant constitutive model in the finite element analysis of SRM, the derived constitutive equation is transformed into an incremental form and integrated into the user subroutine UMAT of the finite element analysis platform ABAQUS. Subsequent to this, a three-dimensional SRM model containing the case, the insulator, and the propellant grain is established. The mechanical response of the grain under thermal and gravitational loads is calculated and analyzed. The results indicate that the stress concentration region in the grain is located at the stress release boot in the forward dome of the motor, where damage occurs. The methods employed in this paper and the conclusions drawn can serve as a reference for evaluating the structural integrity and storage lifespan of the SRM.

Keywords: Solid propellant; Creep, Damage, Constitutive model, Finite element method, Solid rocket motor.

I.   INTRODUCTION

The solid propellant grain is generally subjected to different types of loads from the completion of casting to the end of its combustion task, such as gravity, propellant solidification and cooling, temperature fluctuations, long-term storage, vibration caused by vehicle transportation, pressure, and acceleration during ignition and flight [1].These loads can result in changes in temperature, displacement, strain, and stress of the grain, potentially leading to interface debonding, grain creep, grain dewetting, and crushing. All of these will compromise the structure integrity of the motor and even cause serious accidents [2,3].

When the SRM is in storage, the propellant grain experiences two main associated loads: the heat load due to the temperature difference as the curing temperature equilibrates, and the gravity load. While the stresses caused by these loads are typically minor, their cumulative impact over a long storage could be substantial. As solid propellant exhibits viscoelastic behavior, the grain undergoes creep during storage, leading to deformation of the propellant grain and potentially obstructing the gas discharge process and even blocking the motor nozzle [4], as depicted in Figure 1. Additionally, the storage time of the motor can extend for several decades, and even minor structural damage to the grain will gradually weaken its load-bearing capacity and compromise the structural integrity of the motor.
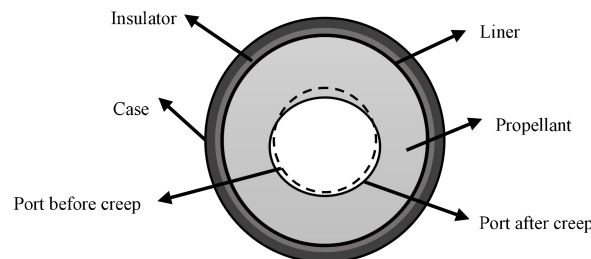

Figure 1: Schematic of Grain Deformation When the SRM is Stored in Horizontal Position

[1] Rocket Force University of Engineering, Xi'an, 710025, China
[2] Rocket Force University of Engineering, Xi'an, 710025, China
[3] Rocket Force University of Engineering, Xi'an, 710025, China
[4] Rocket Force University of Engineering, Xi'an, 710025, China
[5] Rocket Force University of Engineering, Xi'an, 710025, China
[6] Army Engineering University of PLA, Nanjing, 210007, China
*Corresponding author: Yanshen Zhang

Therefore, in order to effectively evaluate the structural integrity of SRM during a long storage, it is particularly important to accurately grasp the laws of propellant creep characteristics. Based on prior experimental findings, the strain-time creep curve of the solid propellant at a constant stress level can be segmented into four distinct phases [5], as illustrated in Figure: (1) immediate elastic deformation phase; (2) initial decelerating creep phase; (3) sustained creep phase; and (4) escalating creep and eventual failure phase.
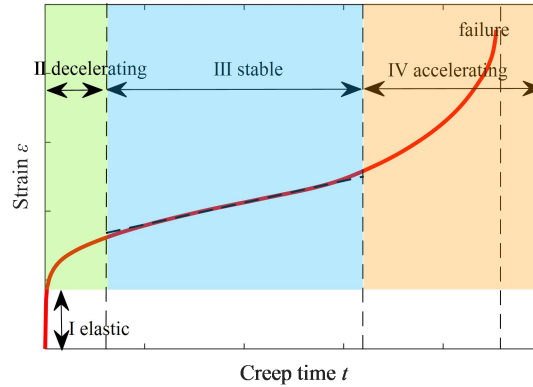

Figure 2: Creep Curve of Propellant under Constant Stress Conditions

Numerous researchers have investigated the creep characteristics of solid propellant. Bihari B et al. [6] employed the Kelvin-Voigt model to analyze the creep characteristics of HTPB solid propellants and studied the variation of model parameters with stress levels. They observed a notable increase in both the spring and damping coefficients with an escalation in stress levels. Wang et al. [7] conducted research on creep experiments of NEPE propellant under eight different stress levels. Luo et al. [8] examined the creep constitutive equations of NEPE propellant through the performance of specimen-level creep tests on NEPE propellant at various load levels. The assessment of the structural integrity of the propellant grain under combined loads was conducted. Wang et al. [9] conducted creep tests on propellant specimens at low stress levels and obtained strain-time curves during the creep process. Hu et al. [10] conducted research on the high-temperature creep mechanical properties of PBT propellant. The results reveal that creep behavior of propellant sample is greatly dependent on the temperature and stress, especially displays obvious loading effect．Cui et al. [11] introduced a creep constitutive model for solid propellant, which considers the Poisson's ratios that vary with time and temperature. Zhang et al. [12,13] formulated computational equations to delineate the strain rate during the second creep phase of double-base solid propellant, drawing from creep testing data. Their study indicated that the generalized Kelvin model could effectively capture the creep behavior of double-base solid propellant. Deng et al. [14] provided a mechanical test procedure for assessing the long-term creep behavior of HTPB propellant. They conducted an analysis of the propellant's long-term creep properties by employing a Modified Burgers model. Zhu et al. [15] conducted a study to examine the impact of stress levels and temperature on the creep behavior of HTPE propellant. However, the constitutive models employed in these investigations offers only a limited representation of the creep behavior of propellant materials. It is unable to capture the accelerating creep phase or anticipate the solid propellant's failure. Therefore, it remains challenging to provide a comprehensive description of the creep behavior of solid propellant.

The creep of the propellant is a long-term process at low stress levels, and some scholars have introduced damage to describe this process. Heller et al. [16] analyzed the impact of environmental factors on the life of the propellant grain using the cumulative damage theory. Nikola et al. [17] evaluated the linear cumulative damage pattern through a large number of HTPB propellant specimens in different but constant stress levels. Wu et al. [18] proposed a Modified Burgers model with damage to describe the entire process of propellant creep at different stress levels. Due to the high stress sensitivity of the constitutive parameters, it can only describe the creep behavior of propellants at a constant stress level.

When the propellant is solidified as the grain in the combustion chamber of a SRM, numerical methods are often needed to analyze it due to the complexity of its structure and the loads. The advancement of computational science and technology has led to a growing use of finite element methods in analyzing complex structures [19]. At present, a large number of scholars have used finite element methods to analyze the mechanical response of the SRM grain under different conditions [20-23]. Some scholars have developed relevant constitutive models and written corresponding programs to calculate the structural integrity of the SRM through commercial finite element platforms in response to the complex mechanical properties of solid propellants [24-27]. However, there

is little numerical analysis on the creep problem of long-term stored SRM grain, as there is still a need for nonlinear numerical constitutive models that can effectively describe the creep process of propellants. In order to accurately analyze the creep characteristic of the solid propellant and its impact on the structural integrity of SRMs during long-term storage, it is essential to construct a reasonable numerical creep constitutive form of propellants. At present, research in this area is not in-depth enough.

To describe the creep properties of HTPB propellant subjected to long-term loading and analyze the response of the grain during storage, a viscoelastic creep damage constitutive model is established based on the generalized Kelvin model and continuum damage mechanics theory. Experimental creep test is conducted on HTPB propellant at varying stress levels to determine the parameters of the constitutive model. Subsequently, the formulated constitutive model is transformed into an incremental format and integrated into the user subroutine UMAT of the finite element analysis platform ABAQUS. To verify the numerical algorithm, two examples including a cylindrical motor and uniaxial constant stress creep test are analyzed. Furthermore, a finite element model of the SRM is constructed to investigate the response of the grain in storage.

II.   CREEP CONSTITUTIVE MODEL

Solid propellant is a kind of polymer with high filling solid particles such as inorganic oxidants and metal additives. Its mechanical properties mainly depend on polymer adhesives, therefore its mechanical properties are mainly manifested as viscoelasticity. When the propellant is subjected to a small load, there is almost no internal damage, therefore, the deformation at this time can be described using a linear viscoelastic constitutive model. The typical structure of the constitutive equation for linear viscoelastic materials in three dimensions can be expressed as follows. [28]:

$$\varepsilon_{ij} = \int_{-\infty}^{t} Y_{ijkl}(t-\tau) \frac{\partial \sigma_{kl}(\tau)}{\partial \tau} d\tau \tag{1}$$

Where, $Y_{ijkl}(t)$ is a creep compliance function.

Assuming that the mechanical properties of the material are isotropic, it can be inferred that $Y_{ijkl}(t)$ is independent of direction and it only has two independent variables. Therefore, its expression is:

$$Y_{ijkl}(t) = \frac{1}{3}\left[Y_2(t) - Y_1(t)\right]\delta_{ij}\delta_{kl} + Y_2(t)\left(\delta_{ik}\delta_{jl} + \delta_{li}\delta_{jk}\right) \tag{2}$$

Where, $Y_1(t)$ and $Y_2(t)$ represent two distinct creep compliance functions that are independent of each other.

The strain tensor ε_{ij} can be separated into two components, spherical strain and deviatoric strain:

$$\varepsilon_{ij}(t) = e_{ij}(t) + \frac{1}{3}\delta_{ij}\hat{\varepsilon}_{kk}(t) \tag{3}$$

Where

$$e_{ij}(t) = \int_{-\infty}^{t} Y_1(t-\tau) \frac{\partial S_{ij}(\tau)}{\partial \tau} d\tau \tag{4}$$

$$\hat{\varepsilon}_{kk} = \int_{-\infty}^{t} Y_2(t-\tau) \frac{\partial \sigma_{kk}(\tau)}{\partial \tau} d\tau \tag{5}$$

Where, $\hat{\varepsilon}_{kk} = \varepsilon_{kk} - 3\alpha^T\theta$, e_{ij} and ε_{kk} represent the deviatoric stress and spherical stress, α^T is the thermal coefficient of expansion, θ represents the variation of temperature, $S_{ij}(t)$ and $\sigma_{kk}(t)$ represent the deviatoric stress and spherical stress respectively.

The creep functions $Y_1(t)$, $Y_2(t)$, shear creep modulus $\chi(t)$, and bulk creep modulus $B(t)$ have the following relationship:

$$Y_1(t) = \frac{1}{2}\chi(t), \quad Y_2(t) = \frac{1}{3}B(t) \tag{6}$$

For the homogeneous isotropic viscoelastic materials, the shear creep modulus $\chi(t)$ and bulk creep modulus $B(t)$ are defined as:

$$\chi(t) = 2(1+v)J(t) \tag{7}$$

$$B(t) = 3(1-2v)J(t) \tag{8}$$

Where, v is the Poisson's ratio, $J(t)$ is the creep compliance under uniaxial tension.

Linear viscoelastic materials are typically characterized by the representation and description of a specific array of elastic and viscous components in various series parallel combinations. The widely used linear viscoelastic models presently include the Maxwell model, Kelvin model, three-parameter Solid model, four-parameter Burgers model, generalized Kelvin model, generalized Maxwell model, and more. Of these, the generalized Kelvin model is frequently applied in describing the creep behavior of materials [29]. As shown in Figure 3, generalized Kelvin model is comprised of an elastic element multiple Kelvin elements connected in series, where E_0 - E_n are the elastic coefficients and η-η_n are the viscosity coefficients.
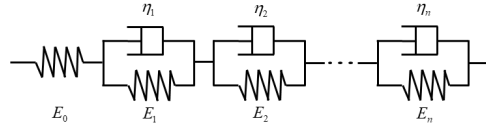

Figure 3: Generalized Kelvin Model

When we use the generalized Kelvin model to describe the viscoelastic properties of solid propellants, their creep compliance can be expressed in the form of Prony series as:

$$J(t) = J_0 + \sum_{n=1}^{N_J} J_n (1 - e^{-\frac{t}{\tau_n}})$$

(9)

Where

$$J_n = \frac{1}{E_n}, \quad \tau_n = \frac{\eta_n}{E_n}$$

(10)

Combined (6), (7), and (8), (4) and (5) can be expressed in the following form:

$$e_{ij}(t) = (1+\nu)\int_{-\infty}^{t} J(t-\tau)\frac{\partial S_{ij}(\tau)}{\partial \tau}d\tau$$

(11)

$$\hat{\varepsilon}_{kk}(t) = (1-2\nu)\int_{-\infty}^{t} J(t-\tau)\frac{\partial \sigma_{kk}(\tau)}{\partial \tau}d\tau$$

(12)

Based on the definition of the Stieltjes convolution integral, (11) and (12) can be represented as shown in the subsequent equation [30]:

$$e_{ij}(t) = (1+\nu)J(\xi)S_{ij}(0) + (1+\nu)\int_{0}^{t} J(t-\tau)\frac{\partial S_{ij}(\tau)}{\partial \tau}d\tau$$

(13)

$$\hat{\varepsilon}_{kk}(t) = (1-2\nu)J(\xi)\sigma_{kk}(0) + (1-2\nu)\int_{-\infty}^{t} J(t-\tau)\frac{\partial \sigma_{kk}(\tau)}{\partial \tau}d\tau$$

(14)

During the process of propellant creep, as time increases, its deformation increases, and the stress-strain relationship exhibits nonlinearity. Therefore, it is essential to develop an accurate model to depict its nonlinear mechanical properties. Schapery [31,32] formulated a nonlinear viscoelastic constitutive equation incorporating damage based on the elastic viscoelastic correspondence principle, and this method is used for reference in this study.

Referring to the form of the constitutive model incorporating damage proposed by Schapery, we introduce pseudo stress instead of real physical stress. For the one-dimensional linear viscoelastic constitutive equation:

$$\varepsilon = J_R \sigma^R$$

(15)

Where, ε can be considered as viscoelastic strain, σ^R is pseudo stress, and it is a convolutional integral form, which is a quantity containing temporal genetic factors:

$$\sigma^R = \frac{1}{J_R}\int_{0}^{t} J(t-\tau)\frac{d\sigma}{\partial \tau}d\tau$$

(16)

Where, J_R represents a reference value of creep compliance. J_R can be chosen arbitrarily, with a common selection being $J_R = 1$.

The form of (15) demonstrates a direct correlation between the linear viscoelastic mechanical response and pseudo stress. In line with the principles of continuous damage mechanics theory, the non-linear mechanical characteristics of materials are linked to the initiation and progression of damage. Empirical investigations have indicated that as damage emerges and advances, the stress-to-strain ratio progressively diminishes. This damage primarily induces a softening effect in the material, leading to a gradual reduction in material rigidity. Consequently, a fundamental element of the non-linear viscoelastic constitutive model of materials involves the

examination of the softening function. Upon integrating the softening function to depict non-linear viscoelasticity, the equation takes on the following form:

$$\varepsilon^d = \frac{\varepsilon}{C(D)} = \frac{\sigma^R}{C(D)}$$

(17)

Where ε^d is the strain of the material after softening due to damage. D is the damage factor, and $C(D)$ is the softening function, which is used to characterize the effect of damage on the flexibility of the propellant. The specific form of $C(D)$ can be obtained from propellant creep test data.

Assuming that the effect of damage on the mechanical properties of propellants is isotropic, according to (13), (14), and (17), the three-dimensional form of viscoelastic creep damage constitutive equation can be formulated as follows:

$$e_{ij}^d(t) = \frac{e_{ij}(t)}{C(D)} = \frac{1}{C(D)}\left[(1+v)J(\xi,t)S_{ij}(0) + (1+v)\int_0^t J(t-\tau)\frac{\partial S_{ij}(\tau)}{\partial \tau}d\tau\right]$$

(18)

$$\hat{\varepsilon}_{kk}^d(t) = \frac{\hat{\varepsilon}_{kk}(t)}{C(D)} = \frac{1}{C(D)}\left[(1-2v)J(\xi,t)\sigma_{kk}(0) + (1-2v)\int_{-\infty}^t J(t-\tau)\frac{\partial \sigma_{kk}(\tau)}{\partial \tau}d\tau\right]$$

(19)

Where, $e_{ij}^d(t)$ and $\hat{\varepsilon}_{kk}^d(t)$ are the deviatoric strain and the spherical strain of the material after softening.

Kachanov [33] believes that the main reason for material performance degradation is the decrease in effective bearing area caused by micro defects. Assuming that the cross-sectional area of the material in a non-destructive state is A and the effective load-bearing area after damage is, the damage factor can be defined as:

$$D = \frac{A-\tilde{A}}{A} = 1-\frac{\tilde{A}}{A}$$

(20)

Ulteriorly, Kachanov assumes a certain relationship between the development of damage and effective stress, and an exponential relationship between the evolution rate of damage and effective stress. Stigh [34] found through experiments that the creep damage change rate of composite solid propellants is related to the damage situation and stress state of the solid propellants as follows:

$$\dot{D} = \frac{1}{N^\beta(\beta+1)}(\frac{\sigma}{1-D})^\beta$$

(21)

Where, β is the exponential of cumulative damage, N is Lebesgue stress norm [35], and its form is as follows:

$$N = \sigma_0 t_0^{1/\beta} = \left[\int_0^{t_f} \sigma(t)^\beta dt\right]^{\frac{1}{\beta}}$$

(22)

Where σ_0 is the reference creep stress, t_0 is the corresponding failure time, and t_f represents the failure time under any stress process. N can be understood as the creep stress required to cause a material to fail per unit time, and its value is independent of loading history, reflecting the inherent properties of the material.

III. CREEP TEST OF HTPB PROPELLANT SPECIMENS

A. Test Method

Constant stress creep tests are conducted on HTPB propellant specimens at varying stress levels to determine the creep compliance coefficient and damage parameters in the proposed constitutive model and verify its effectiveness. The test specimens, consisting of 88% solid filled particles (Ammonia Perchloric acid and aluminum powder), 12% Hydroxyl-terminated polybutadiene, bonding agent, and other additives, were prepared and stored at dry natural temperature for a certain time. These specimens were shaped into a dumbbell shape according to the standard GJB770B-2005, as illustrated in Figure 4. The production of the test pieces adhered to the following requirements: (1) The absence of visible defects such as impurities, holes, and cracks. (2) The operation process carried out in an environment with a relative humidity not exceeding 50%.
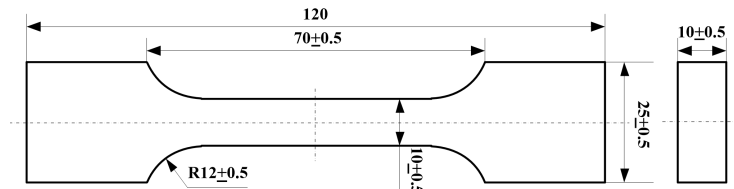
Figure 4: Dimensions and Physical Schematic Diagram of Propellant Specimens

Due to the moisture-absorbing characteristics of the propellant, the test was conducted in a high-low temperature-humidity test chamber. The assembly of the test equipment is shown in Figure 5(a). Figure 5(b) is a schematic diagram of the test equipment placed in the test chamber. The test chamber ensures stability of the experimental temperature and humidity. During the experiment, the temperature is set at 20℃ and the humidity is controlled below 50%. The deformation of the propellant specimen is obtained by calculating the variation in displacement between the top face of the lower fixture and the scale. The test process was recorded by a high-definition camera outside the observation window of the environmental box, and the tensile strain of the propellant specimen was subsequently obtained through image processing and data processing.
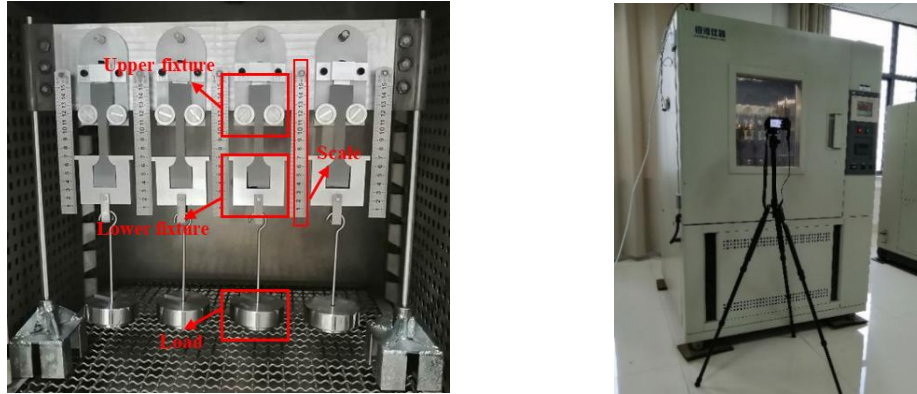
(a) Propellant Specimens and Fixtures   (b) Test Chamber and Observation Devices

Figure 5: Test Equipment and Observation Devices

B. Test Results and Analysis

Figure 6 illustrates the mean creep behavior of HTPB solid propellant specimens subjected to varying stress levels. The creep response of the propellant specimens exhibit a characteristic four-phase progression when subjected to loads ranging from 0.25MPa to 0.4MPa. Initially, the specimens undergo immediate elastic deformation upon application of the load. This is followed by a decay creep phase where the rate of strain diminishes progressively with time. Upon transitioning to the creep steady state phase, the strain rate stabilizes and remains constant. Finally, in the escalating creep phase, the propellant experiences significant weakening of its mechanical properties due to the increased accumulation rate of damage. This results in a rapid increase in the strain rate and eventual damage to the propellant. However, under a load of 0.05MPa, the creep process of the propellant only encompasses the first three stages within the testing period due to the low stress level.
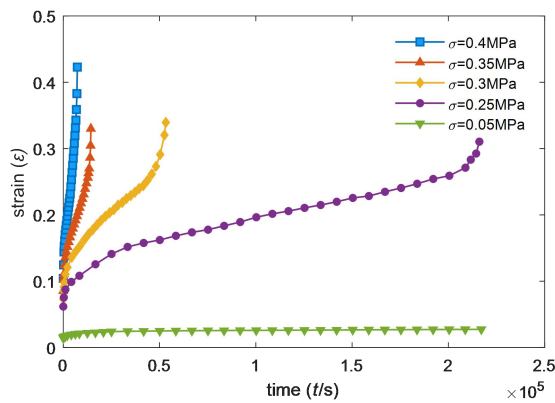

Figure 6: Creep Curves of Specimens under Different Stress Levels

C. Method of Obtaining the Model Parameters

The creep test conducted in this article adopts static load, and the stress level of the propellant specimen is a constant value. According to the damage evolution model, the relationship between propellant loading stress, loading time, and damage can be obtained by integrating (21):

$$D = 1 - \left[1 - \left(\frac{\sigma_s}{N} \right)^{\beta} t \right]^{\frac{1}{\beta+1}}$$

(23)

Where σ_s is the stress level and t is the loading time.

When $D = 1$, the propellant failure occurs. According to (24), the correlation between the failure time t_f and the stress level σ_s is:

$$\left(\frac{\sigma_s}{N}\right)^\beta t_f = 1 \tag{24}$$

Equation (24) can be further rewritten as:

$$\ln t_f = \beta\left(\ln N - \ln \sigma_s\right) \tag{25}$$

According to (25), the least squares method is used to fit the different stress levels and corresponding average failure time of the specimen, with the resulting damage parameters presented in Table 1. Figure 7 shows the curve of stress level vs. time. The graphical representation illustrates a near-linear relationship between the logarithm of stress levels and the logarithm of failure time, suggesting the efficacy of the cumulative damage model in forecasting the fracture time of propellant specimens subjected to varying stress levels.
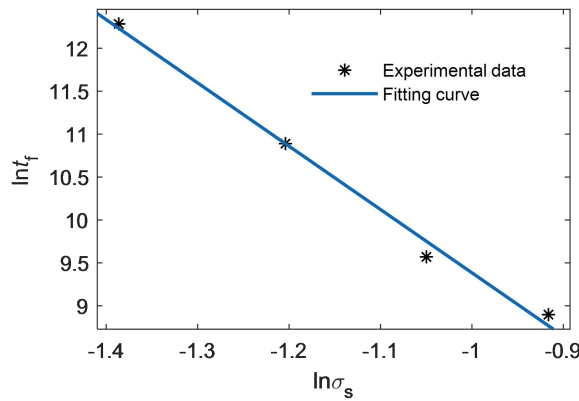

Figure 7: Curve of Stress level (logarithmic) vs. time (logarithmic)

Table 1: Fitting Results of Damage Parameters

N	β	R^2
1.314	7.371	0.992

The loading time of the propellant at low stress levels (0.05MPa) is 2.2×10^5s, the obtained damage parameter values are substituted into (23), and it is found that after loading at a stress level of 0.05MPa, the damage growth is only 7.4542e-06. Therefore, it can be approximated that the propellant do not undergo damage during this loading process. The time-dependent strain curve at this stress level can be used to fit the Prony series creep compliance parameters. The fitting parameters are presented in Table 2, while the corresponding fitting curve is depicted in Figure 8. The figure illustrates that at low stress levels, the creep curve derived from the generalized Kelvin model closely aligns with the experimental curve, with a fitting judgment coefficient of $R^2=0.982$.

Table 2: Fitting Results of Creep Compliance Parameters

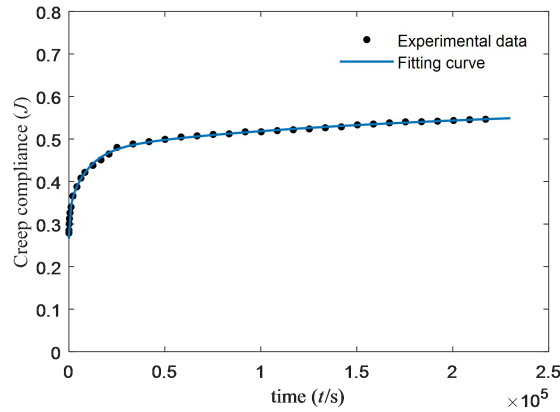| i	τ_i/s	J_i/(MPa^{-1})
0	\	0.2657
1	10	0.01532
2	100	0.01801
3	1000	0.04396
4	10000	0.1273
5	100000	0.05469
6	1000000	0.14308

Figure 8: Creep Compliance Curve Fitting at Low Stress Levels (σ=0.05MPa)

In the process of propellant creep under high stress levels, as damage accumulates, the stress-strain relationship of the propellant will exhibit nonlinearity. We investigate the numerical relationship between the damage value and the softening function, and substitute the obtained damage parameters and creep compliance coefficient into (17) to obtain the corresponding relationship between the propellant damage value and the softening function. Due to the rapid increase in propellant damage and strain during the accelerated creep failure stage, in order to reduce fitting errors, the parameter fitting curves of the damage and softening functions only consider the first three stages of creep. The variation curve of propellant softening function with respect to damage under different stress levels is shown in Figure 9. The illustration demonstrates that when the propellant is not damaged, the softening function is approximately 1, indicating that the mechanical properties of the propellant are close to linear viscoelasticity at this time. As the damage accumulates during the creep process, the softening function gradually decreases, reflecting a decrease in the stiffness of the propellant caused by the damage, resulting in a certain degree of softening. By parameter fitting, the form of the softening function is determined as:

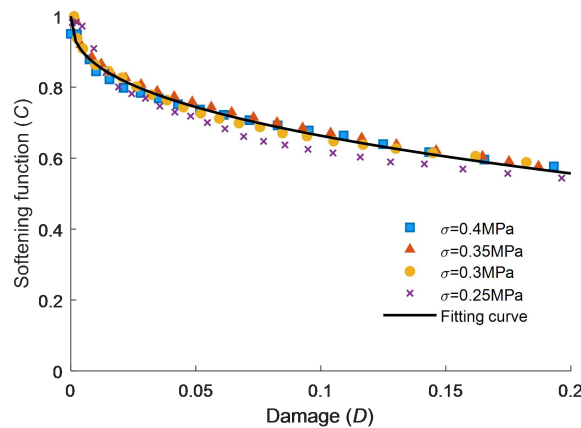$$C(D) = 1 - 0.8381D^{0.3959}$$

(26)

Figure 9: Curve of Softening Function vs. Damage

D. Model Validation

At this point, all parameters in the creep damage constitutive equation have been obtained. To verify the rationality and accuracy of this constitutive form, the stress levels of 0.25-0.4MPa have been substituted into the model. Figure 10 illustrates a juxtaposition of the theoretical curve with the experimental curve, showcasing the alignment between the proposed creep damage constitutive equation and the observed deformation characteristics during the propellant's creep process. The theoretical curve effectively mirrors the experimental curve across various stress levels and loading conditions. It should be noted that due to the strong nonlinearity of stress and strain in the accelerated failure stage during the creep process, there are some deviations from the test data at this stage.
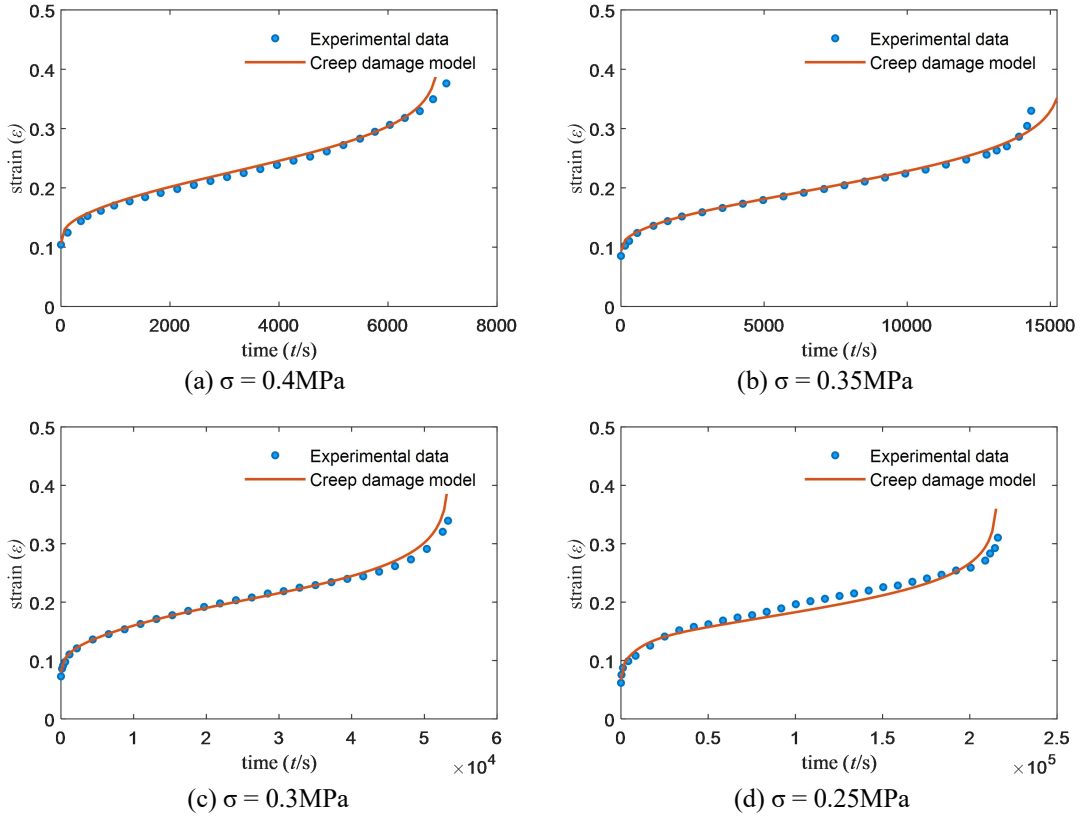
(a) σ = 0.4MPa

(b) σ = 0.35MPa

(c) σ = 0.3MPa

(d) σ = 0.25MPa

Figure 10: Comparison of Theoretical Curves and Experimental Data under Different Stress Levels

IV. APPLICATION METHOD OF CONSTITUTIVE EQUATIONS

A. Incremental Form of Constitutive Equation

In order to apply the proposed constitutive model to the finite element analysis of commercial software, we use UMAT subroutine to realize data exchange with ABAQUS main solver. The behavior of viscoelastic materials is characterized by a deformation history that is influenced by the load history. Typically, addressing such scenarios necessitates the application of the incremental finite element method for problem resolution. Consequently, the constitutive equation must be reformulated into an incremental representation to align with this computational approach.

Firstly, the analysis time interval $[0, t]$ is decomposed into several subtime increment steps, that is, $[0, t_1]$, $[t_1, t_2]$, $[t_2, t_3], \ldots, [t_m, t_{m+1}], \ldots, [t_n, t]$. For the constitutive equation shown ins (18) and (19), the incremental form within the time increment step $[t_m, t_{m+1}]$ can be expressed as:

$$\Delta\varepsilon_{ij}^d(t_{m+1}) = \Delta e_{ij}^d(t_{m+1}) + \frac{1}{3}\delta_{ij}\Delta\varepsilon_{kk}^d(t_{m+1}) \tag{27}$$

Where

$$\Delta e_{ij}^d(t_{m+1}) = \frac{C[D(t_m)]\Delta e_{ij}(t_{m+1}) - \Delta C[D(t_{m+1})]e_{ij}(t_m)}{C^2[D(t_{m+1})]} \tag{28}$$

$$\Delta\varepsilon_{kk}^d(t_{m+1}) = \frac{C[D(t_m)]\Delta e_{ij}(t_{m+1}) - \Delta C[D(t_{m+1})]e_{ij}(t_m)}{C^2[D(t_{m+1})]} \tag{29}$$

From (28), it can be seen that in order to obtain the numerical value of $\Delta e_{ij}^d(t_{m+1})$ and $\Delta\varepsilon_{kk}^d(t_{m+1})$, it is necessary to solve for $\Delta e_{ij}(t_{m+1})$, $\Delta\varepsilon_{kk}(t_{m+1})$, and $\Delta D(t_{m+1})$.

As for $\Delta e_{ij}(t_{m+1})$, we convert (13) to the following form:

$$\Delta e_{ij}(t_{m+1}) = (1+\nu)\left[\Delta e_{ij}^I(t_{m+1}) + \Delta e_{ij}^{II}(t_{m+1}) + \Delta e_{ij}^{III}(t_{m+1})\right] \tag{30}$$

Where

$$\Delta e_{ij}^{\mathrm{I}}(t_{m+1}) = \left[J(t_{m+1}) - J(t_m) \right] S_{ij}(0) \tag{31}$$

$$\Delta e_{ij}^{\mathrm{II}}(t_{m+1}) = \int_{t_m}^{t_{m+1}} J(t_{m+1} - \tau) \frac{\partial S_{ij}(\tau)}{\partial \tau} d\tau \tag{32}$$

$$e_{ij}^{\mathrm{III}}(t_{m+1}) = \int_0^{t_m} \left[J(t_{m+1} - \tau) - J(t_m - \tau) \right] \frac{\partial S_{ij}(\tau)}{\partial \tau} d\tau \tag{33}$$

Substituting (9) into (31),yields:

$$\Delta e_{ij}^{\mathrm{I}}(t_{m+1}) = \sum_{n=1}^{N_J} J_n (e^{-\frac{t_m}{\tau_n}} - e^{-\frac{t_{m+1}}{\tau_n}}) S_{ij}(0) \tag{34}$$

Substituting (9) into (32),yields:

$$\Delta e_{ij}^{\mathrm{II}}(t_{m+1}) = \int_{t_m}^{t_{m+1}} \left[J_0 + \sum_{n=1}^{N_J} J_n (1 - e^{-\frac{t_{m+1}-\tau}{\tau_n}}) \right] \frac{\partial S_{ij}(\tau)}{\partial \tau} d\tau$$
$$= \int_{\xi_m}^{\xi_{m+1}} \left[J_0 + \sum_{n=1}^{N_J} J_n (1 - e^{-\frac{t_{m+1}-\tau}{\tau_n}}) \right] \frac{\partial S_{ij}(\tau)}{\partial \xi'} d\xi' \tag{35}$$

Moreover, by assuming that the deviatoric stress tensor changes linearly with reduced time during the increment, $\Delta e_{ij}^{\mathrm{II}}(t_{m+1})$ can be obtained:

$$\Delta e_{ij}^{\mathrm{II}}(t_{m+1}) = \left[J_0 + \sum_{n=1}^{N_J} J_n \left[1 - \beta_n^J(\Delta t_{m+1}) \right] \right] \Delta S_{ij}(t_{m+1}) \tag{36}$$

Where

$$\beta_n^J(\Delta t) = \frac{\tau_n^J}{\Delta t} \left(1 - e^{-\frac{\Delta t}{\tau_n}} \right) \tag{37}$$

Similarly, substituting (9) into (33) yields:

$$e_{ij}^{\mathrm{III}}(t_{m+1}) = \sum_{n=1}^{N_J} J_n \int_0^{t_m} \left[(e^{-\frac{t_m-\tau}{\tau_n}} - e^{-\frac{t_{m+1}-\tau}{\tau_n}}) \right] \frac{\partial S_{ij}(\tau)}{\partial \tau} d\tau$$
$$= \sum_{n=1}^{N_J} J_n \left(1 - e^{-\frac{\Delta t_{m+1}}{\tau_n}} \right) \int_0^{t_m} e^{-\frac{t_m-\tau}{\tau_n}} \frac{\partial S_{ij}(\tau)}{\partial \tau} d\tau \tag{38}$$

Thus, we rewrite (38) as:

$$e_{ij}^{\mathrm{III}}(t_{m+1}) = \sum_{n=1}^{N_J} J_n \left(1 - e^{-\frac{\Delta t_{m+1}}{\tau_n}} \right) \eta_{ij}^n(t_{m+1}) \tag{39}$$

Where

$$\eta_{ij}^n(t_{m+1}) = \int_0^{t_m} \left[(e^{-\frac{t_m-\tau}{\tau_n}} - e^{-\frac{t_{m+1}-\tau}{\tau_n}}) \right] \frac{\partial S_{ij}(\tau)}{\partial \tau} d\tau$$
$$= \int_{t_{m-1}}^{t_m} e^{-\frac{t_m-\tau}{\tau_n}} \frac{\partial S_{ij}(\tau)}{\partial \tau} d\tau + \int_0^{t_{m-1}} e^{-\frac{t_m-\tau}{\tau_n}} \frac{\partial S_{ij}(\tau)}{\partial \tau} d\tau$$
$$= \beta_n^E(\Delta t_m) \Delta S_{ij}(t_m) + e^{-\frac{\Delta t_m}{\tau_n^E}} \eta_{ij}^n(t_m) \tag{40}$$

For $\Delta \hat{\varepsilon}_{kk}(t_{m+1})$, we use the same method to convert (14) to the following form:

$$\Delta \hat{\varepsilon}_{kk}(t_{m+1}) = (1 - 2\nu) \left[\Delta \varepsilon_{kk}^{\mathrm{I}}(t_{m+1}) + \Delta \varepsilon_{kk}^{\mathrm{II}}(t_{m+1}) + \Delta \varepsilon_{kk}^{\mathrm{III}}(t_{m+1}) \right] \tag{41}$$

Where

$$\Delta \varepsilon_{kk}^{\mathrm{I}}(t_{m+1}) = \sum_{n=1}^{N_J} J_n (e^{-\frac{t_m}{\tau_n}} - e^{-\frac{t_{m+1}}{\tau_n}}) \sigma_{kk}(0) \tag{42}$$

$$\Delta \varepsilon_{kk}^{\mathrm{II}}(t_{m+1}) = \left[J_0 + \sum_{n=1}^{N_J} J_n \left[1 - \beta_n^J(\Delta t_{m+1}) \right] \right] \Delta \sigma_{kk}(t_{m+1}) \tag{43}$$

$$\varepsilon_{kk}^{\mathrm{III}}(t_{m+1}) = \sum_{n=1}^{N_J} J_n \left(1 - e^{-\frac{\Delta t_{m+1}}{\tau_n}} \right) \eta_{kk}^{n}(t_{m+1})$$

(44)

Where

$$\eta_{kk}^{n}(t_{m+1}) = \beta_n^{J}(\Delta t_m) \Delta \hat{\varepsilon}_{kk}(t_m) + e^{-\frac{\Delta t_m}{\tau_n}} \eta_{kk}^{n}(t_m)$$

(45)

Due to the lack of obvious directionality in solid propellants, the damage of the specimen does not exhibit obvious directionality before obvious cracks appear in the three-dimensional stress state. Therefore, it is approximately believed that the damage is isotropic in the three-dimensional stress state. The evolution equation of the internal variable of the damage in the three-dimensional stress state, according to (21), is:

$$\dot{D} = \frac{1}{N^{\beta}(\beta+1)} \left(\frac{\sigma^{eq}}{1-D} \right)^{\beta}$$

(46)

Where σ^{eq} is the equivalent stress. Von Mises stress is used to determine the yield of materials, including solid propellant in the three-dimensional stress state. Therefore, it is considered as the equivalent stress to characterize the damage evolution process of materials.

According to (48), the damage increment from t_m to t_{m+1} is:

$$\Delta D(t_{m+1}) = \int_{t_m}^{t_{m+1}} \dot{D} dt = \int_{t_m}^{t_{m+1}} \frac{1}{N^{\beta}(\beta+1)} \left(\frac{\sigma^{eq}}{1-D} \right)^{\beta} dt$$

(47)

Integrate(47) as:

$$\Delta D(t_{m+1}) = 1 - \left\{ \left[1 - D(t_m) \right]^{\beta+1} - \frac{\Delta t_{m+1}}{N^{\beta}} \sigma_m^{eq\beta} \right\}^{\frac{1}{\beta+1}}$$

(48)

B. Tangent Stiffness Matrix for Constitutive Equations

When the Newton Iterative method is used in Abaqus to solve the overall balance equation, it is necessary to provide the consistent tangent stiffness matrix, i.e., the Jacobian matrix, to form the overall Stiffness matrix of the system in the overall balance equation. The consistent tangent stiffness matrix can ensure that the external iteration process of the Abaqus/Standard solver reaches the secondary convergence rate. For the discrete constitutive increment form, the Jacobian matrix is typically defined as the partial derivative of the stress increment corresponding to the strain increment within the current step of the increment.

In order to avoid resolving Jacobian matrix at each iteration and reduce the amount of calculation, the modified N-R iterative method is used and the initial Jacobian matrix is used for calculation. In the discrete time domain, the tangent stiffness can be mathematically represented as:

$$C_{ijkl}(t_{m+1}) = \frac{\partial \Delta \sigma_{ij}(t_{m+1})}{\partial \Delta \varepsilon_{kl}^{d}(t_{m+1})}$$

(49)

According to the incremental equation given in (28), (29) and combined with (36), (43), the tangent stiffness tensor components at t_{m+1} can be obtained, which are:

$$C_{1111}(t_{m+1}) = \frac{\partial \Delta S_{11}(t_{m+1})}{\partial \Delta \varepsilon_{11}^{d}(t_{m+1})} + \frac{1}{3} \frac{\partial \Delta \sigma_{kk}(t_{m+1})}{\partial \Delta \varepsilon_{11}^{d}(t_{m+1})}$$
$$= \frac{C^2 \left[D(t_{m+1}) \right]}{3C \left[D(t_m) \right] \hat{J}(t_{m+1})} \left[\frac{2}{1+\nu} + \frac{1}{1-2\nu} \right]$$

(50)

$$C_{1122}(t_{m+1}) = \frac{\partial \Delta S_{11}(t_{m+1})}{\partial \Delta \varepsilon_{22}^{d}(t_{m+1})} + \frac{1}{3} \frac{\partial \Delta \sigma_{kk}(t_{m+1})}{\partial \Delta \varepsilon_{22}^{d}(t_{m+1})}$$
$$= \frac{C^2 \left[D(t_{m+1}) \right]}{3C \left[D(t_m) \right] \hat{J}(t_{m+1})} \left[\frac{1}{1-2\nu} - \frac{1}{1+\nu} \right]$$

(51)

$$C_{1212}(t_{m+1}) = \frac{\partial \Delta S_{12}(t_{m+1})}{\partial \Delta \gamma_{12}^d(t_{m+1})}$$

$$= \frac{C^2[D(t_{m+1})]}{2C[D(t_m)]\hat{J}(t_{m+1})(1+v)} \tag{52}$$

Where

$$\hat{J}(t_{m+1}) = J_0 + \sum_{n=1}^{N_J} J_n \left[1 - \beta_n^J(\Delta \xi_{m+1})\right] \tag{53}$$

For isotropic materials, it is easy to know that other components have the following relationships:

$$C_{2222}(t_{m+1}) = C_{3333}(t_{m+1}) = C_{1111}(t_{m+1}) \tag{54}$$

$$C_{2233}(t_{m+1}) = C_{1133}(t_{m+1}) = C_{1122}(t_{m+1}) \tag{55}$$

$$C_{2323}(t_{m+1}) = C_{1313}(t_{m+1}) = C_{1212}(t_{m+1}) \tag{56}$$

Except for the components with values given above, all other components of the tangent stiffness tensor have zero values.

V. APPLICATIONS IN FINITE ELEMENT ANALYSIS

A. Verification by Structural Analysis of a Pipe Construction

For the constitutive model proposed in this paper, when the damage is ignored and $D=0$, it will degenerate into a linear viscoelastic constitutive model. In this situation, the analytical expression of the linear viscoelastic problem can be used to compare with the finite element solution obtained by the method in this paper, and then the algorithm and program given can be preliminarily verified. A cylindrical SRM model with a shell under uniformly distributed internal pressure on the inner surface has been established. as shown in Figure 11(a). It can be simplified as a plane strain problem. The geometric dimensions of the solid motor are as follows: inner diameter of the grain a=200mm, outer diameter b=397mm, and shell thickness h_s =3mm. Uniform internal pressure load $P(t) = P_0(1 - e^{-kt})$ is applied to the inner surface of the motor. Due to its geometric structure and load symmetry, a 1/4 structure of the model could be used for analysis, and the 4-node rectangular isoparametric element is used to partition it, thus a finite element mesh model has been established as shown in Figure 11(b).

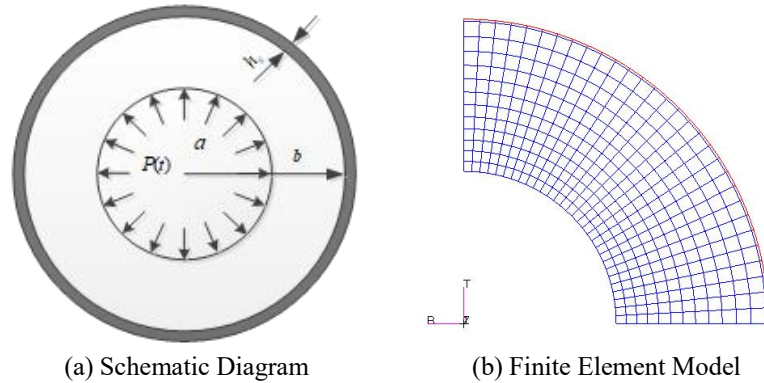(a) Schematic Diagram   (b) Finite Element Model

Figure 11: Schematic Diagram and Finite Element Model of Cylindrical SRM

For the above viscoelastic plane strain problem, the corresponding Analytical expression of strain is [15]:

$$\varepsilon_r(r,t) = -\chi\left(\frac{b^2}{r^2} + 1\right)\frac{P_0 f_J(t)}{E_\infty} + \alpha(1+v)\left[(1-2v) - \frac{a^2}{r^2}\right]\frac{\kappa b}{h_s E_s}P(t) \tag{57}$$

$$\varepsilon_\theta(r,t) = \chi\left(\frac{b^2}{r^2} - 1\right)\frac{P_0 f_J(t)}{E_\infty} + \alpha(1+v)\left[(1-2v) + \frac{a^2}{r^2}\right]\frac{\kappa b}{h_s E_s}P(t) \tag{58}$$

Where, ε_r is radial strain, ε_θ is circumferential strain, is equilibrium modulus, J_∞ is equilibrium compliance, E_s is tensile and compression modulus of shell, v_s and v are respectively Poisson's ratio of shell and propellant, and:

$$\lambda = \frac{b}{a}, \quad \eta = \frac{2(1-v)}{1+(1-2v)\lambda^2}, \quad \chi = \frac{(1-2v)(1+v)}{1+(1-2v)\lambda^2} \tag{59}$$

$$\alpha = \frac{\lambda^2}{\lambda^2 - 1}, \quad \kappa = \frac{2(\lambda^2 - 1)(1 - \nu)}{\left[1 + (1 - 2\nu)\lambda^2\right]^2 (1 + \nu)}\left(1 - \nu_c^2\right) \tag{60}$$

$$f_J(t) = \left(1 - e^{-kt}\right) + \sum_{i=1}^{N_J} \frac{J_i}{J_\infty}\left(1 + \frac{e^{-kt} - k\tau_i e^{-t/\tau_i}}{k\tau_i - 1}\right) \tag{61}$$

Where J_∞ is equilibrium compliance.

In the calculation process, the internal pressure load parameters P0=0.15MPa, k=0.0002, and the calculation time t=20000s were taken. The creep compliance of the propellant was calculated using the data in Table 2. Other material parameters are given in Table 3.

The finite element solution and analytical expression in this paper are respectively used for comparative analysis. The strain curve of the inner surface of the grain over time under internal pressure loading is depicted in Figure 12. In addition, in order to compare and analyze the distribution of the results obtained by the two methods, the radial variation curves of stress and strain in the circular tube when loaded to 20000 seconds are given, as shown in Figure 13.

Table 3: Material Parameters of Various Components of SRMs

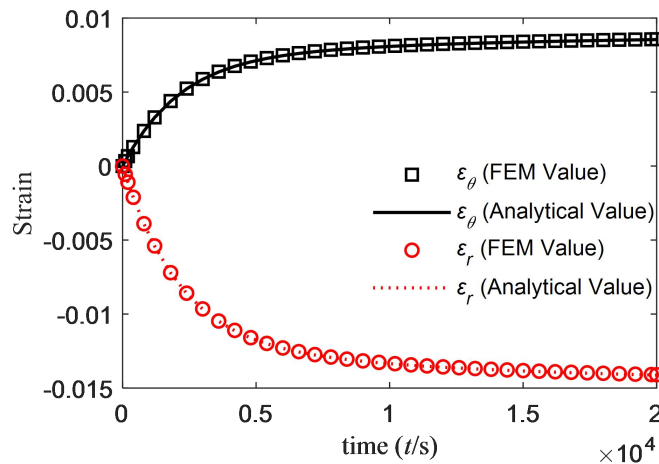| Material parameters	Components		
	Case	Insulator	Grain
E /MPa	2.1×10^5	6.2	—
α^T /(1/K)	1.1×10^{-5}	9.8×10^{-5}	9.25×10^{-5}
ν	0.3	0.495	0.495
ρ /(kg/m^3)	7800	1200	1800

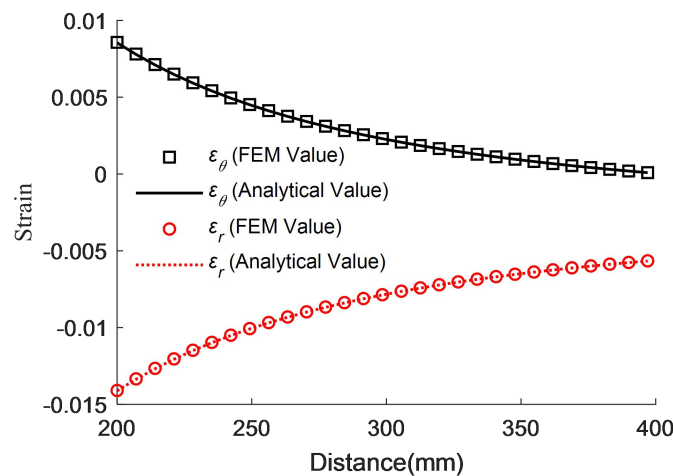Figure 12: Curve of Strain of the Inner Surface vs. Loading Time

Figure 13: Curve of Strain along the Radial Direction after Loading for 20000 Seconds

The comparison between the finite element solution derived using the methodology outlined in this study and the corresponding analytical solution for the aforementioned issues, as depicted in Figure 12 and Figure 13,

demonstrates a high level of concordance. This indicates that when the constitutive model degenerates to the linear viscoelastic one, the corresponding algorithm presented in this paper has high accuracy.

B.   Verification by Uniaxial Constant Stress Loading Test

Let us further consider viscoelastic structural analysis with damage. As shown in Figure 14, the analysis model corresponds to a HTPB propellant specimen which is subjected to uniaxial constant stress tensile loading. The propellant specimen model is 50mm long and has a rectangular cross-section of 10mm×10mm. Along with this model, the damage parameters and the creep compliance parameters of the propellant specimen are provided in Table 1 and Table 2, respectively. The tensile stress applied to the specimen are set to 0.25MPa and 0.3MPa respectively.
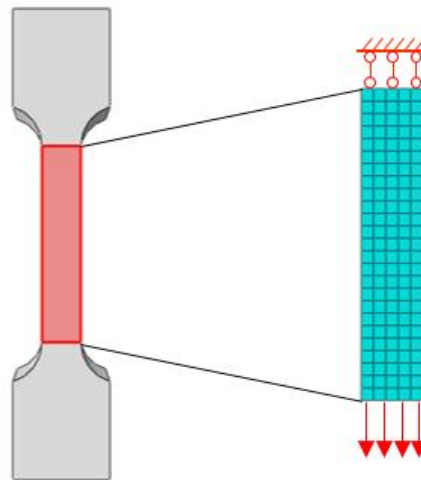

Figure 14: Finite Element Model of Propellant Specimens under Uniaxial Tension

Figure 15 illustrates a comparison between the finite element analysis outcomes and the theoretical curves. The mechanical response of the finite element outcomes, derived through utilizing the creep damage constitutive material subroutine in the numerical simulation program, exhibits consistent behavior with the changes observed in the theoretical model curve. Although some deviation is observed during the creep failure stage, the overall fit is satisfactory.
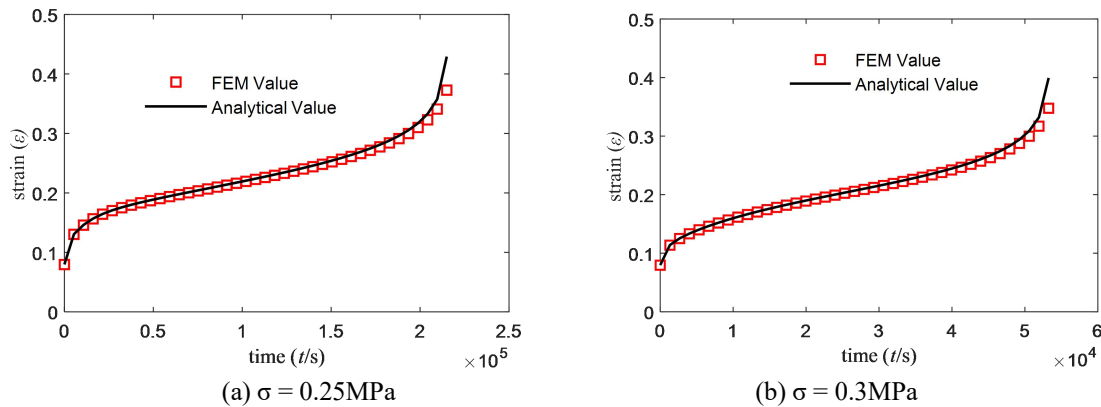

(a) σ = 0.25MPa   (b) σ = 0.3MPa

Figure 15: Comparison of Simulation Results with Theoretical Curves and Experimental Results

Figure 16 displays the progression of damage curves for the solid propellant subjected to varying levels of stress loading. In the early stages of the loading process, the growth rate of damage is relatively small. As the loading time increases, the growth rate of damage gradually accelerates while still approximating a linear growth pattern. However, as the loading time continues to increase and the damage of the propellant reaches around 0.2, the creep process of the solid propellant enters the accelerated creep failure stage. During this stage, the growth rate of the solid propellant damage rapidly increases until the specimen is destroyed. Furthermore, the results derived from the finite element analysis align well with the theoretical values. Thus, the constitutive model proves to be effective in accurately reflecting the creep process and damage evolution of HTPB propellant.
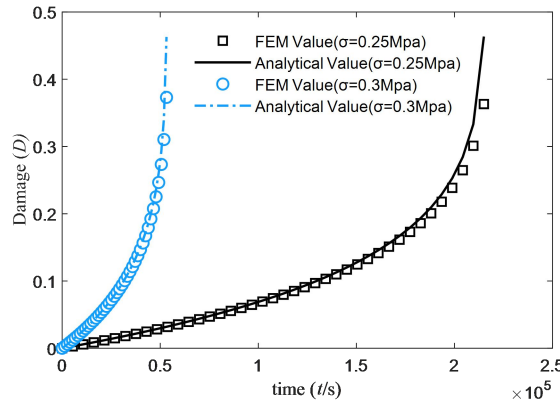
Figure 16: Curves of Damage Evolution under Different Stress Levels

C. Structural Analysis of an SRM

The storage process of a SRM can be analyzed using a three-dimensional finite element model. In this finite element model, the motor initially cools down from 331.15K to 298.15K and maintains this temperature for 72 hours. Afterward, the motor is placed horizontally for a year of storage. The model, shown in Figure 17, is built in Abaqus and has dimensions of 4200mm in length, 1800mm in outer diameter, and 500mm in inner diameter. The motor consists of a shell, an insulator, and a propellant grain. Stress release boots are present inside the insulator at the front and rear of the motor. Several simplifications were made in the modeling process considering the complex structure of the motor. These simplifications include omitting the structure of the front and rear frame and motor nozzle, assuming tight bonding between the shell and the grain, and neglecting the presence of gas in the middle. The calculation process does not account for interface debonding. Due to its geometric structure and load symmetry, a 1/2 structure of the model is used for analysis. The built motor's finite element model consists of 227,600 elements and 248,862 nodes.
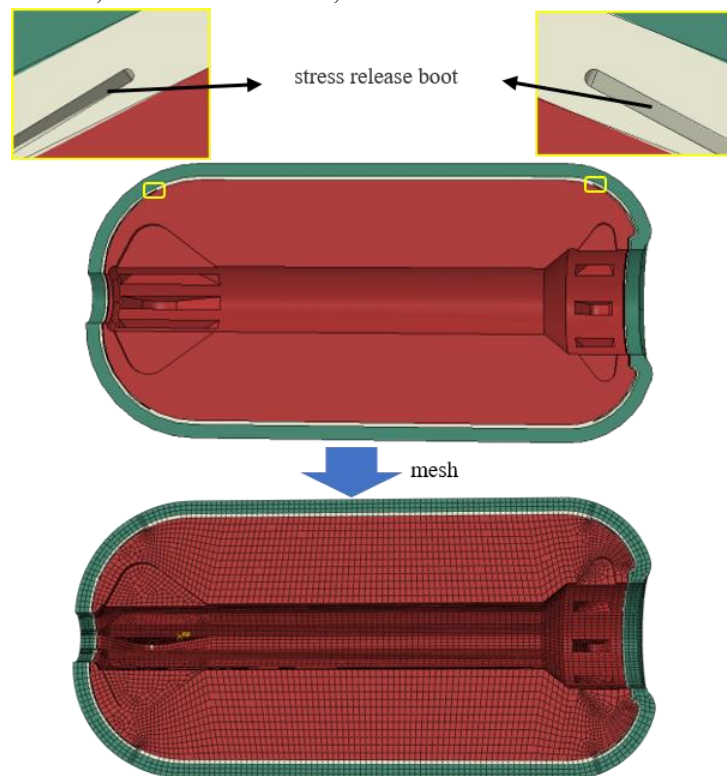

Figure 17: Finite Element Model of SRM

The peak Von Mises stress exhibited by the propellant grain after solidification and cooling is 0.1338 MPa. Subsequently, a reduction in the maximum Von Mises stress of the grain is observed during the storage period, with the stress level diminishing to 0.1088 MPa following one year of horizontal storage. Although the stress level of the inner hole of the grain is relatively high, about 0.06 MPa, the maximum stress point is located near the stress release boot in forward dome of SRM, as shown in Figure 18(a). This is due to the fact that the

expansion coefficient of the grain is much greater than that of the shell, causing it to experience tensile force near the stress release boot when the temperature drops. Additionally, the front end of the grain sags under gravity load, resulting in further tensile force at this position. The combination of these loads leads to stress concentration in this specific area. The damage distribution cloud map of the engine grain after one year of storage, presented in Figure 18(b), indicates that the damage to the grain is primarily situated near the root of the stress release boot between the grain and the insulator, with a maximum damage value of 0.055.
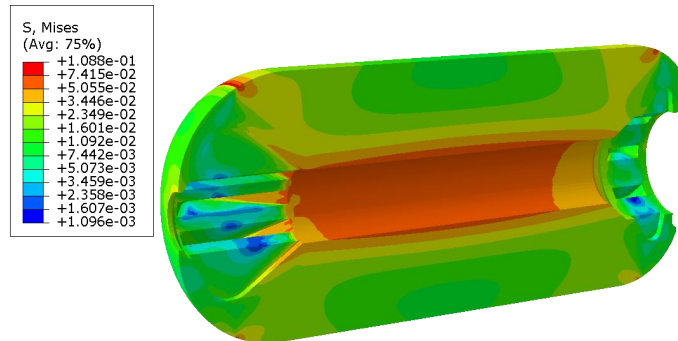

(a)Schematic of Von Mises Stress
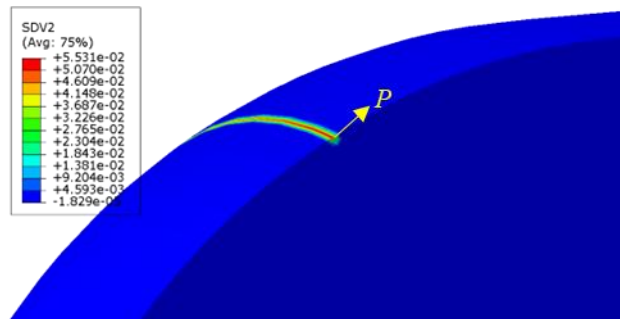
(b) Schematic of Damage

Figure 18: Finite Element Calculation Results of SRM

Point P has been marked as the maximum damage location in Figure 18(b) and we analyzed the mechanical response over time at this location. Figure 19 shows the curves of the mises stress and damage over time at point P during storage after grain cooling. From Figure 19(a), it can be observed that the mises stress of point P rapidly decreases at the beginning of storage of the SRM, reaching 0.1184MPa after approximately 3 days. This decrease is attributed to the relaxation of the propellant caused by its viscoelasticity after curing and cooling. As the storage process continues, the mises stress continues to gradually decrease. This phenomenon can be attributed to the progressive reduction in rigidity and rise in deformation of the solid propellant as it sustains damage over the course of storage. Consequently, this alleviates local stress concentration. The calculation results indicate that propellant damage during storage is beneficial for the long-term storage of SRM as it helps reduce local stress concentration. Additionally, based on Figure 19(b), it can be inferred that the damage value at point P shows a linear relationship with the storage time.
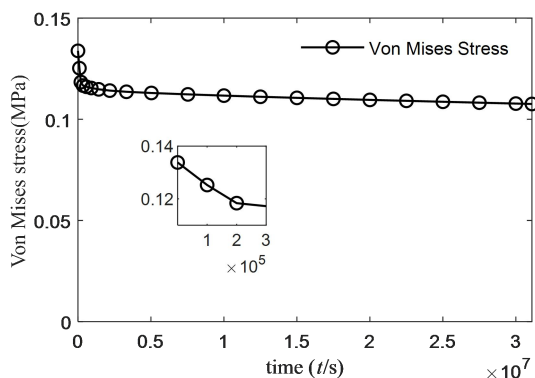
(a) Curves of Von Mises Stress vs. Time
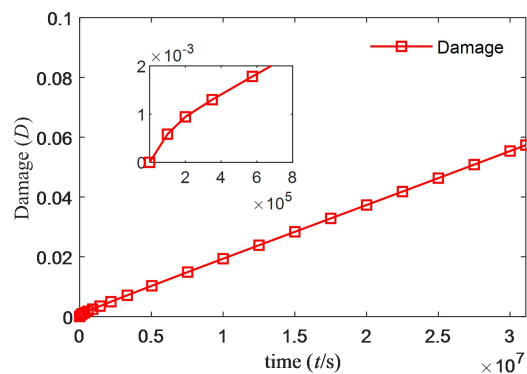
(b) Curves of Damage vs. Time

Figure 19: Curves of Mechanical Response vs. Time at Point P

VI. Conclusions

Based on the research results, the following conclusions can be drawn:

(1) At low stress levels (0.05 MPa), HTPB propellants primarily demonstrate linear viscoelasticity. Conversely, when subjected to high stress levels (0.25 MPa - 0.4 MPa), the creep curve of HTPB propellants displays typical four-stage characteristics and significant nonlinearity. Through the application of the cumulative damage theory, it becomes feasible to anticipate the creep failure time of HTPB propellants under various stress levels.

(2) The finite element analysis results of the horizontal storage of the SRM show that the stress concentration zone is located at the stress release boot in forward dome of the motor, and the damage growth rate at this location is relatively fast. As the storage time increases, the damage to the propellant grain increases approximately linearly, and the propellant at the damaged location gradually softens, which helps to reduce local stress concentration and is beneficial for the long-term storage of SRM.

The methods employed in this paper and the conclusions drawn can serve as an important reference for evaluating the structural integrity and storage lifespan of the SRM.

Acknowledgment

References

[1] Renganathan K, Rao B N, Jana M K, Slump Estimation of Cylindrical Segment Grains of a Typical Rocket Motor under Vertical Storage Condition. Trends in Applied Sciences Research. 2006, 1(1): 97-104

[2] Bills K W JR, Wiegand J H, The application of an integrated structural analysis to the prediction of reliability. Annals of Reliability and Maintainability, USA: Annals of Reliability and Maintainability, 1970.

[3] Marimuthu R, Nageswara Rao B, Development of efficient finite elements for structural integrity analysis of solid rocket motor propellant grains. International Journal of Pressure Vessels & Piping. 2013, 111: 131-145.

[4] Naseem H, Yerra J, Murthy H, et al, Ageing Studies on AP/HTPB Based Composites Solid Propellants. Energetic Materials Frontiers. 2021, 2(2): 111-124.

[5] Cao W, Chen K, Tan X, et al, A novel damage-based creep model considering the complete creep process and multiple stress levels. Computers and geotechnics. 2020, 124: 103599.

[6] Bihari B, Rao N, Gupta M, et al, A Study on Creep Behavior of Composite Solid Propellants Using Kelvin-Voigt Model. Central European Journal of Energetic Materials. 2017, 14(3): 742-756.

[7] Wang J X, Fang Q Z, Sha B L, Investigation on the creep models of the NEPE solid propellant, Mechanics of Advanced Materials and Structures. 2022, DOI:10.1080/15376494.2022.2163728.

[8] Luo Y, Sha B, Hou X, Study on constitutive equations of HTPB propellant. Solid Rock Technol. 2020, 43(6): 799-807.

[9] Wang X, Zhao R, Lu H, et al, Creep behavior of HTPB propellant charges and factors affecting it. Chinese Journal of Explosives & Propellants. 2021, 44(3): 399-406.

[10] Hu Y, Zuo H, Zheng Q, et al, Creep Behavior of Composite Solid Propellant Based on PBT at High Temperature. Solid Rock Technol. 2018, 41(1): 41-46.

[11] Cui H R, Zhang B, Shen Z B, Creep Constitutive Model of the Solid Propellants Considering the Viscoelastic Poisson's Ratio. Solid Rock Technol. 2019, 42(4): 447-450.

[12] Zhang J B, Ju Y T, Zhou C S, Research on Creep Characteristics of the Double-Base Solid Propellant. Advanced Materials Research. 2012, 591: 1062-1066.

[13] Zhang J B, Lu B J, Gong S F, Comparative analyses of creep models of a solid propellant. Materials Science and Engineering. 2018, 359(1): 012050.

[14] Deng K W, Li H Y, Jie X, et al, 2022) Long-Term and Short-Term Creep Characteristic Analysis for HTPB Propellant. Propellants, Explosives, Pyrotechnics. 2022, 47(9):1-10.

[15] Zhu G, Liu S, Liu W, Zheng M, et al, Creep behaviors of HTPE propellants. Propellants, Explosives, Pyrotechnics. 2023, 48: e202200295.

[16] Heller R A, Singh M P, Zibdeh H, Environmental Effects on Cumulative Damage in Rocket Motors. Journal of Spacecraft & Rockets. 2015, 22(2): 149-155.

[17] Nikola Gligorijević, Saša Živković, Sredoje Subotić, et al, Effect of Cumulative Damage on Rocket Motor Service Life. Journal of Energetic Materials. 2015, 33(4): 229-259.

[18] Wu X, Zheng J, Xu J S, et al, Research on Creep Damage Model of HTPB Solid Propellant. Chinese Journal of Explosives & Propellants. 2023, 46(3): 260-265.

[19] Kudela J, Matousek R. Recent advances and applications of surrogate models for finite element method computations: a review. Soft Computing, 2022, 26(24): 13709-13733.

[20] Aksoy T, Altintaş B, Olğar T, et al, Probabilistic Sensitivity Analysis of Solid Propellant Mechanical Properties for the Structural Assessment Under Ignition Pressurization. 2019 9th International Conference on Recent Advances in Space Technologies. IEEE. 2019: 59-64.

[21] Zalewski R, Wolszakiewicz T, Response of a complex solid rocket propellant on axial loadings under various operational conditions. Przemysl Chemiczny. 2016, 95(12): 2452-2455.

[22] Guo X, Zhang J T, Zhang M, et al, Effects of liner properties on the stress and strain along liner/propellant interface in solid rocket motor. Aerospace Science and Technology. 2016, 58: 594-600.

[23] Chyuan S W, Studies of Poisson's ratio variation for solid propellant grains under ignition pressure loading. International journal of pressure vessels and piping. 2003, 80(12): 871-877.

[24] Ha K, Schapery R A, A three-dimensional viscoelastic constitutive model for particulate composites with growing damage and its experimental validation. International Journal of Solids and Structures. 1998, 35(26-27): 3497-3517.

[25] Hinterhoelzl R M, Schapery R A, FEM implementation of a three-dimensional viscoelastic constitutive model for particulate composites with damage growth. Mechanics of Time-Dependent Materials. 2004, 8(1): 65-94.

[26] Tunc B, Ozupek S, Implementation and validation of a three-dimensional damaging finite strain viscoelastic model. International Journal of Solids and Structures. 2016, 102(12): 275-285.

[27] Tunc B, Ozupek S, Constitutive modeling of solid propellants for three-dimensional nonlinear finite element analysis. Aerospace Science and Technology. 2017, 69(8): 290-297.

[28] Christensen, R.M, Theory of Viscoelasticity: An Introduction. Academia Press, New York. 1982.

[29] Peng G, Chen Z, Chen J, Research on Rock Creep Characteristics Based on the Fractional Calculus Meshless Method. Advances in Civil Engineering. 2018, 2018(2): 1-6.

[30] Cui H R, Tang G J, Shen Z B, A three-dimensional viscoelastic constitutive model of solid propellant considering viscoelastic Poisson's ratio and its implementation, European Journal of Mechanics/A-Solids. 2017, 61: 235-244.

[31] Schapery R A, On viscoelastic deformation and failure behavior of composite materials with distributed flaws, Advances in Aerospace Structures and Materials-AD-01. ASME, New York. 1981: 5-20.

[32] Schapery R A, Models for damage growth and fracture in nonlinear viscoelastic Particulate composites. Proc. Nineth U.S. National Congress of Applied Mechanics, Book No.H00229, ASME, New York. 1982: 237-245.

[33] Kachanov L M, On the time to failure under creep condition. Isv. Akad. Nauk. USSR. Otd. Tekhxl Nauk. 1958, 8:26-31.

[34] Stigh U, Continuum damage mechanics and the life-fraction rule. Journal of Applied Mechanics. 2006, 73: 702-704.

[35] Laheru K L, Development of a generalized failure criterion for viscoelastic materials. Journal of Propulsion and Power. 1992, 8(4): 756-759.